Grasping periodic trend and rate-determining step for S-modified metals of metal sulfides deployable to produce ·OH via H_2O_2 cleavage

Jongsik Kim[a,*], Yun Jeong Choe[a], Sang Hoon Kim[a,b], Seung-Cheol Lee[c,d], Satadeep Bhattacharjee[d]

[a] *Materials Architecturing Research Center, Korea Institute of Science and Technology, Seoul, 02792, South Korea*
[b] *Division of Nano & Information Technology in Korea Institute of Science and Technology (KIST) School, University of Science and Technology (UST), Daejeon, 34113, South Korea*
[c] *Electronic Materials Research Center, Korea Institute of Science and Technology, Seoul, 02792, South Korea*
[d] *Indo-Korea Science and Technology Center, Korea Institute of Science and Technology, Bengaluru, 500065, India*

ABSTRACT

Iron sulfides are fascinating catalytic phases because these include S-modified $Fe^{\delta+}$ ($\delta \leq 2$) species functioning as H_2O_2 activators to form ·OH used for oxidatively degrading aqueous contaminants (e.g., phenol). As an initial step for locating S-modified metal species ($M^{\delta+}$) that outperform $Fe^{\delta+}$ in catalytic H_2O_2 cleavage, hexagonal metal sulfides (MS) were synthesized using Mn, Fe, Co, Ni, and Cu to understand electric potential-assisted H_2O_2 scission kinetics on $M^{\delta+}$ species. $Ni^{\delta+}$ species were found to show the greatest ·OH productivity among all $M^{\delta+}$ species studied, mainly resulting from the Lewis acidic nature of $Ni^{\delta+}$ species adequate to expedite the liberation of ·OH species. This was partially evidenced by H_2O_2 activation/phenol degradation runs on $M^{\delta+}$ species, wherein initial H_2O_2 activation rate ($-r_{H2O2,0}$) or initial phenol degradation rate ($-r_{PHENOL,0}$) of $Ni^{\delta+}$ species was 3–9 times those of the other $M^{\delta+}$ species. $Ni^{\delta+}$ species, therefore, were located in the middle of the volcano-shaped curve plotting $-r_{H2O2,0}$ (or $-r_{PHENOL,0}$) versus the type of $M^{\delta+}$. Kinetic assessment of $M^{\delta+}$ species under fine-tuned reaction environments also showed that regardless of varying H_2O_2 concentrations, $M^{\delta+}$ species were found to retain their $-r_{H2O2,0}$ values in the absence of electric potentials. Conversely, $M^{\delta+}$ species could enhance $-r_{PHENOL,0}$ values at larger electric potentials, where greater energies were likely exerted on $M^{\delta+}$ species. This indeed corroborated that ·OH desorption from $M^{\delta+}$ species was the rate-determining step to direct catalytic H_2O_2 scission. In addition to heterogeneous catalytic nature of $Ni^{\delta+}$ species in fragmenting H_2O_2, outstanding H_2O_2 scission ability provided by $Ni^{\delta+}$ species could also compensate for their moderate catalytic stability at pH-neutral condition.

1. Introduction

Hydrogen peroxide (H_2O_2) is a central chemical shuttle to carry various oxidizers including ·O_2^-, ·OOH, and ·OH, all of which can serve to degrade contaminants present in aquifer solids or groundwater (Fig. 1(c)–(e)) [1–3]. H_2O_2, however, can find itself challenging to be deployed in such applications unless H_2O_2 is cleaved efficiently to provide large quantity of ·OH with the strongest standard oxidation potential (i.e., ~2.8 eV for ·OH; ≤ ~1.8 eV for ·O_2^- and ·OOH) [1–3]. High ·OH productivity driven by H_2O_2 cleavage was reported to be achievable through the use of well-tailored catalytic scissors, among which S-modified, Fe-bearing surfaces have shown promises in catalyzing H_2O_2 fragmentation rapidly and heterogeneously [4,5]. In particular, electron (e^-)-abundant surface Fe species innate to FeS_2 (i.e.,

$Fe^{\delta+}$, where $\delta \leq 2$) were unveiled to provide unique Lewis acidic feature adequate to cleave H_2O_2 via $Fe^{\delta+}$ redox-mediated heterogeneous catalysis (Fig. 1(c)–(e)) [4–6]. As a way to better utilize $Fe^{\delta+}$ species inherent to FeS_2, we suggested the use of alternative catalytic phases such as Fe_3S_4 and Fe_7S_8 because these phases intrinsically incorporate $Fe^{\delta+}$ vacancies open to H_2O_2, as is not the case with FeS_2 [6]. Our reaction runs indeed manifested the advantages of Fe_3S_4/Fe_7S_8 over FeS_2 such as promoted ·OH productivity and increased rates to decompose a model contaminant (phenol) with reduced leaching of surface $Fe^{\delta+}$ species [6].

However, scientific achievements in H_2O purification depicted above have been confined to the use of S-doped Fe oxides [7,8], FeS_2 [4,5], and their analogues as catalysts [6], while primarily focusing on the parametric optimization of their reaction conditions to better
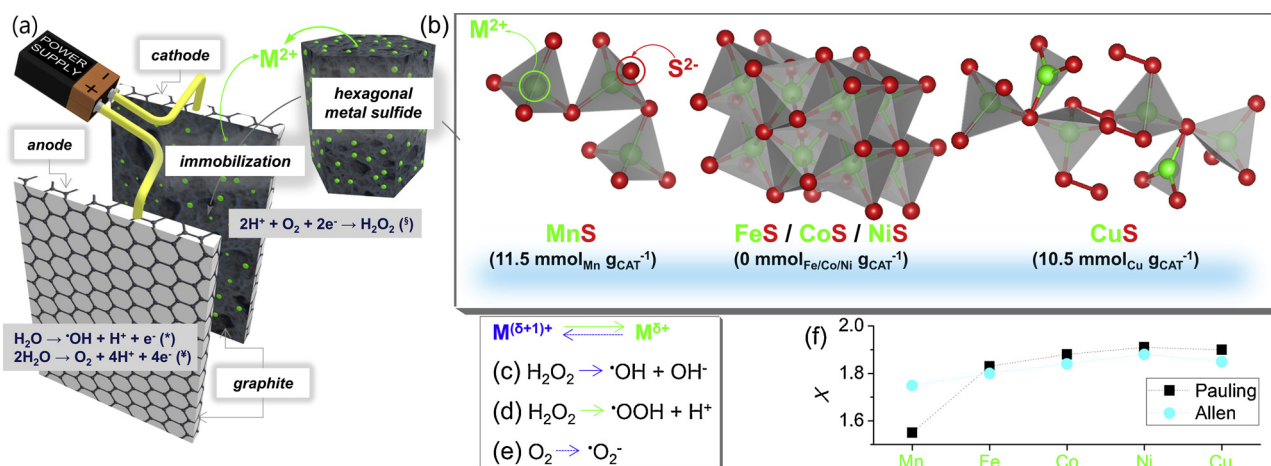
Fig. 1. Illustration of (a) electric potential-driven catalytic production of radicals used to decompose phenol and (b) atom connectivities of the metal sulfides utilized to catalytically generate radicals. (c–e) Elementary steps suggested to depict heterogeneous catalytic evolution of ˙OH, ˙OOH, and ˙O_2^- radicals, all of which involve the redox of S-modified metal species. In $M^{\delta+}$ and $M^{(\delta+1)+}$, M denotes metal, whereas δ denote oxidation state of metal ($\delta \leq 2$). Blue, dotted arrows in (c) and (e) indicate the oxidation of $M^{\delta+}$ to form $M^{(\delta+1)+}$ upon e^- donation. Green, solid arrows in (d) indicate the reduction of $M^{(\delta+1)+}$ to form $M^{\delta+}$ upon e^- acceptance. (f) Electro-negativities (X) of metal species used to construct the metal sulfides.

catalyze H_2O_2 scission. Active sites inherent to these catalysts were also elaborated via their mechanistic investigations [4–8]. These studies suggested plausible pathways to catalyze H_2O_2 cleavage, most of which, however, were postulated based on rate constants of elementary steps given in literature resources [4–8]. Therefore, it is left as essential questions to-date that 'Can we explore catalytic nature of other metal sulfides desired to fragment H_2O_2 and enhance H_2O_2 scission performance over Fe sulfide?' and 'Can we suggest the rate-determining step to cleave H_2O_2 for these catalysts via kinetic investigation?' Here, we envisioned to screen transition metal species used to construct metal sulfides, investigate their H_2O_2 scission kinetics by regulating reaction environments, and locate the optimum metal sulfide favorable to maximize catalytic ˙OH productivity.

For this purpose, we initially selected the simplest yet synthetically feasible metal sulfide structure defined as MS (M: metal; S: sulfur) [9–13]. M was varied from Mn, Fe, Co, Ni, to Cu based on their ubiquities in conjunction with their locations found in the periodic trend (i.e., identical period; different group). The motivations beyond the selection of the MS structures are summarized as follows: These can be readily obtained via hydrothermal or solvothermal synthesis [9–13]. In addition, these are built in a hexagonal crystal system [9–13] and therefore were expected to circumvent any geometrical effect on their catalytic performance. Furthermore, these are barely porous [9–13] and thus were anticipated to minimize any textural effect, when examining their catalytic consequences.

However, albeit choosing the identical crystal system for fair comparison among the MS catalysts, their atom connectivities should be regarded as one of vital factors to contemplate for finding the periodic trend of the MS catalysts to cleave H_2O_2 (Fig. 1(b)). This was because the amount of Lewis acidic sites was greatly dependent on the co-ordination geometry of metal species innate to the MS catalysts, as demonstrated previously [6]. MnS consists of corner-sharing, *tetrahedral* MnS_4^{6-} motifs, where all $Mn^{\delta+}$ sites are Lewis acidic and accessible to H_2O_2 (~11.5 $mmol_{Mn}\ g_{CAT}^{-1}$) [14]. CuS also adopts such a geometry that *triangular* CuS_3^{4-} clusters corner-shared with *tetrahedral* CuS_4^{6-} motifs are coupled to provide ~10.5 mmol of Lewis acidic $Cu^{\delta+}$ sites accessible to H_2O_2 per a gram of CuS [15]. It was likely conclusive that both MnS and CuS could show better ˙OH productivity compared to the other metal sulfides (i.e., FeS, CoS, and NiS) because these catalysts constitute of edge-sharing, *octahedral* MS_6^{10-} clusters inaccessible to H_2O_2 [16]. However, this statement could be valid only if all metal sulfides were defect-free.

Additional pivotal factor that should be considered is electro-

negativities of metal species included in the MS catalysts (Fig. 1(f)). This was because metal sulfides with greater electro-negativities of metals could provide smaller Lewis acidic strengths [17,18], which in turn could affect the interactions between the metal species and H_2O_2. S has larger electro-negativity than metal species (~2.6) and thus tends to extract e^- from the metals, as conjectured based on our previous studies on metal phosphide [17] and metal vanadate [18]. Based on the electro-negativities of the metals investigated in this study, $Mn^{\delta+}$ species were expected to show the most e–deficient, the greatest Lewis acidic strength among all metals present in the MS catalysts studied. This could potentially allow for $Mn^{\delta+}$ sites of MnS to bind with H_2O_2 species in the strongest manner among all metal sites present in the MS catalysts. This was in contrast to $Ni^{\delta+}$ sites of NiS because Ni has the greatest electro-negativities among all metals, potentially leading to the weakest interactions between $Ni^{\delta+}$ sites and H_2O_2, when forming NiS. Hence, it was highly likely that FeS, CoS, or CuS could outperform MnS and NiS due potentially to moderate interactions of $Fe^{\delta+}$, $Co^{\delta+}$, or $Cu^{\delta+}$ sites with H_2O_2 species during H_2O_2 fragmentation.

Two competing trends predicted above were quite discrepant and therefore further justified the need to investigate the periodic trend of the MS catalysts for H_2O_2 cleavage to clarify 'Which kind of metal sulfide does provide the most desired catalytic surface beneficial to fragment H_2O_2?' and 'What is the major factor for such surface to show the greatest H_2O_2 scission performance?' In this study, we utilized electro-Fenton reaction system as an answering tool for these questions, where a bare graphite and a catalyst-coated graphite served as an anode and a cathode, whereas electric potential input initiated the catalytic H_2O_2 cleavage in the presence of aqueous Na_2SO_4 electrolyte (Fig. 1(a)) [3,6]. Our choice of electro-Fenton system was based on its major benefits including 1) simple set-up with a small electric potential required for its operation, 2) sufficient H_2O_2 generated via anodic H_2O oxidation (¥ in Fig. 1(a)) followed by cathodic O_2 reduction (§ in Fig. 1(a)), 3) increased likelihood to reduce $M^{(\delta+1)+}$ to $M^{\delta+}$ by e^- for the continuous usage of $M^{\delta+}$ to produce ˙OH, and 4) a catalytic surface on the cathode, leading to its promoted contact with H_2O_2 generated on the cathode [3,6]. Along with characterization experiments, a series of reaction runs with the use of phenol as a model for aqueous contaminants were also conducted under controlled conditions. The resulting kinetic data was rigorously analyzed to answer aforementioned questions.

2. Methods

2.1. Synthesis of metal sulfides

Metal sulfides were hydro-thermally or solvothermally synthesized according to slightly modified procedures reported elsewhere [9–13]. For the synthesis of MnS, a mixture composed of 11.5 mmol of $MnCl_2 \cdot 4H_2O$ (JUNSEI, 99.0 %), 34.5 mmol of $C_3H_7NO_2S$ (L-cysteine, JUNSEI, 98.0%), and 100 mL of deionized was placed in a 150 mL Teflon acid digestion sleeve, heated at 200 °C for 12 h, filtered using deionized water and C_2H_5OH (ethanol, DAESUNG, 94.5%), and dried at 110 °C overnight [9]. For the synthesis of FeS, a mixture consisting of 12 mmol of $FeCl_2 \cdot 4H_2O$ (Sigma-Aldrich, 99.99%), 24 mmol of CH_3CSNH_2 (thioacetamide, WAKO, 98.0%), and 80 mL of $C_2H_8N_2$ (ethylenediamine, Sigma-Aldrich, ≥ 99.5%) was put inside a 150 mL Teflon acid digestion sleeve, heated at 180 °C for 96 h, filtered using deionized water and C_2H_5OH, and annealed at 500 °C for an hour under a N_2 atmosphere with a ramping rate of 5 °C min^{-1} and a total flow rate of 200 mL min^{-1} prior to being cooled to 25 °C [10]. For the synthesis of CoS, a mixture constituting of 5 mmol of $Co(NO_3)_2 \cdot 6H_2O$ (JUNSEI, 97.0%), 10 mmol of CH_3CSNH_2, and 100 mL of $C_2H_8N_2$ was located inside a 150 mL Teflon acid digestion sleeve, heated at 180 °C for 24 h, filtered using deionized water and C_2H_5OH, and dried at 110 °C overnight [11]. For the synthesis of NiS, a mixture composed of 4 mmol of $NiSO_4 \cdot 6H_2O$ (JUNSEI, 99.0%), 8 mmol of H_2NCSNH_2 (thiourea, JUNSEI, 98.0%), 60 mL of deionized water, and 30 mL of $C_2H_6O_2$ (ethylene glycol, DAEJUNG, 99.0%) was situated inside a 150 mL Teflon acid digestion sleeve, heated at 200 °C for 24 h, filtered using deionized water and C_2H_5OH, and dried at 110 °C overnight [12]. For the synthesis of CuS, 5 mmol of $Cu(NO_3)_2 \cdot 3H_2O$ (JUNSEI, 99.0%), 25 mmol of H_2NCSNH_2, and 80 mL of deionized were placed in a 150 mL Teflon acid digestion sleeve, heated at 150 °C for 24 h, filtered using deionized water and C_2H_5OH, and dried at 110 °C overnight [13].

2.2. Characterizations

N_2 physisorption experiments of the catalysts were carried out using ASAP 2010 (Micromeritics) at 77 K. X-ray diffraction (XRD) patterns of the catalysts were recorded using D8 Advance (Bruker) at a scan speed of 2 s per step and a step size of 0.02° per step with monochromatic Cu K_α radiation (λ = 1.54 Å). High-resolution transmission electron microscopy (HRTEM) images and selected area electron diffraction (SAED) patterns of the catalysts were acquired using FEI (Titan 80-300™) at 300 keV. CO-pulsed chemisorption experiments of the catalysts were performed using AutoChem II (Micromeritics) at 40 °C [6,17,19–22]. X-ray photoelectron (XP) microscopy experiments of the catalysts were conducted using PHI 5000 VersaProbe, while employing adventitious carbon located at binding energy of 284.6 eV as a reference. Atomic absorption spectrometry (AAS) and inductively coupled plasma-optical emission spectrometry (ICP-OES) experiments were performed using ICS 3000 (Thermo Fisher Scientific) and iCAP 6500 DUI (Thermo Fisher Scientific) for the quantification of metal and S species leached from the catalysts during the reaction runs. Electric conductivities of the reaction solutions were recorded using HI98191 (HANNA) during the initial 2 h of the reaction runs. The quantity of H_2O_2 (Sigma-Aldrich, 29.0–32.0 wt. %, H_2O_2 basis) evolved or consumed during the reaction runs was monitored using ultraviolet-visible spectrometer (Cary 100 UV–vis) at 454 nm while employing $C_{14}H_{12}N_2$ (2,9-dimethyl-1,10-phenanthroline, Sigma-Aldrich, ≥ 98%) as a probe molecule, which was reported by K. Kosaka and co-workers [23]. Conversion of H_2O_2 (X_{H2O2}) during the reaction run was evaluated using Eq. (1), where $C_{H2O2,0}$ and C_{H2O2} denote the initial H_2O_2 concentration and the H_2O_2 concentration at a specific reaction time, respectively. Initial H_2O_2 scission rate of the catalyst (-$r_{H2O2,0}$) was evaluated using Eq. (2), as we reported previously [6]. k_{APP} denotes apparent, lumped reaction rate constant obtained through fitting of

reaction data to pseudo-1st-order kinetic model. $N_{H2O2,0}$ and N_{CO} denote moles of H_2O_2 used for the reaction run and the amount of CO-accessible sites present in the catalyst, respectively.

$$X_{H2O2}(\%) \frac{C_{H2O2,0} \ (mol \ L^{-1}) - C_{H2O2} \ (mol \ L^{-1})}{C_{H2O2,0}(mol \ L^{-1})} \times 100 \tag{1}$$

$$- r_{H2O2,0}(\min^{-1}) = \frac{k_{APP}(\min^{-1}) \times N_{H2O2,0}(mol)}{0.2g_{CAT} \times N_{CO}(mol_{co} \ g_{CAT}^{-1})} \tag{2}$$

The quantity of phenol (C_6H_5OH, DAEJUNG, 99%) consumed during the reaction runs was monitored using high-performance liquid chromatography (LC-20 A, Shimadzu) via reverse phase chromatography method, as reported previously [6]. Conversion of phenol (X_{PHENOL}) during the reaction runs was evaluated using Eq. (3), where $C_{PHENOL,0}$ and C_{PHENOL} denote the initial phenol concentration and the phenol concentration at a specific reaction time, respectively. Initial phenol degradation rate of the catalyst (-$r_{PHENOL,0}$) was evaluated using Eq. (4), as we reported previously [6]. $N_{PHENOL,0}$ denotes moles of phenol used for the reaction run.

$$X_{PHENOL}(\%) = \frac{C_{PHENOL,0}(mol \ L^{-1}) - C_{PHENOL}(mol \ L^{-1})}{C_{PHENOL,0}(mol \ L^{-1})} \times 100 \tag{3}$$

$$- r_{PHENOL,0}(\min^{-1}) = \frac{k_{APP}(\min^{-1}) \times N_{PHENOL,0}(mol)}{0.2g_{CAT} \times N_{CO}(mol_{co} \ g_{CAT}^{-1})} \tag{4}$$

2.3. Reactions

Reactions were carried out according to the protocols slightly modified based on our previous works [6,24,25]. Prior to the reaction runs, 0.2 g of the catalyst was mixed with 0.2 g of 7 wt. % binder $((CH_2CF_2)_n$ Poly (vinylidene fluoride), average M_w ˜180,000, average M_n ˜71,000, Sigma-Aldrich) dissolved in C_5H_9NO (N-Methyl-2-pyrrolidone, Sigma-Aldrich, ≥ 99%). The resulting catalyst slurry was then immobilized on a graphite plate used as a cathode (Groupe Carbone Lorraine, grade 2124) with a coated area of 3 cm × 4 cm and dried at 110 °C overnight. After that, a coated cathode as well as a bare graphite utilized as anode was positioned vertically with a gap of 3 cm inside a 150 mL beaker before adding a reaction solution into the beaker. The reaction was initiated by stirring the reaction solution at 240 rpm and at 25 °C without or with electric input of 1 V (32.4 (± 2.4) mA), 2 V (24.4 (± 1.5) mA), or 3 V (14.7 (± 0.9) mA). For a typical H_2O_2 evolution run, 100 mL of pH-neutral, aqueous solution containing 0.2 mol of Na_2SO_4 (Sigma-Aldrich, ≥ 99%) was employed. For a typical H_2O_2 scission run, 100 mL of pH-neutral, aqueous solution containing 0.2 mol of Na_2SO_4 and 1.5 mmol (or 4 mmol) of H_2O_2 was employed. For a typical phenol degradation run, 100 mL of pH-neutral, aqueous solution containing 0.2 mol of Na_2SO_4 and 0.1 mmol of phenol was employed. For the quantification of H_2O_2 or phenol during the reaction runs, 1 mL reaction aliquot was taken from the reaction solution at pre-determined time, quenched using 1 μL of CH_3OH, and filtered using 0.45 μm sized-PES syringe filter (Whatman®). The catalyst post the reaction run was detached from the cathode, collected through vacuum filtration over a Whatman filter paper (Grade 5, pore size: 2.5 μm), washed with 300 mL of deionized water and 200 mL of C_2H_5OH, and dried at 110 °C overnight. All reaction runs were replicated more than three times to ensure the reaction performance and to accumulate the catalyst for the subsequent recycle run. In a typical filtration run, the cathode coated with the catalyst was removed from the reaction solution after an hour of the reaction run and the reaction solution was subjected to vacuum-filtration over Celite®545 (~20 g). The resulting, filtered reaction solution further experienced electro-Fenton run to keep monitoring phenol concentration versus time.
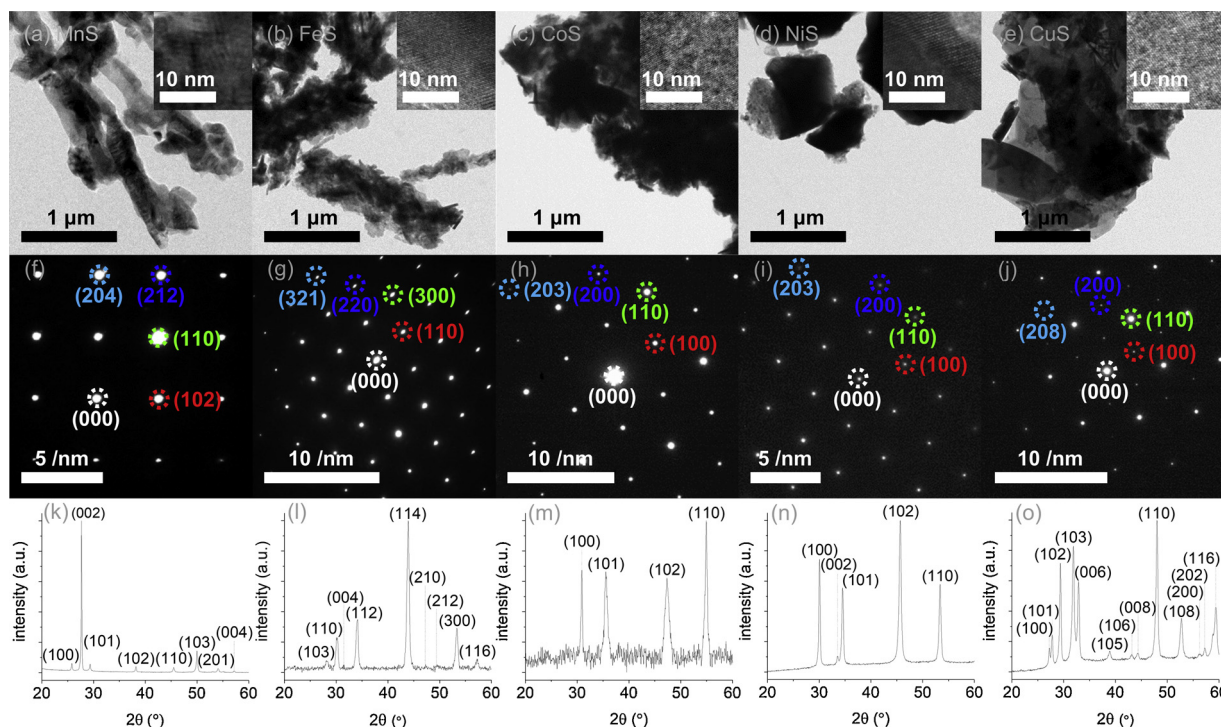
Fig. 2. HRTEM images, SAED, and XRD patterns of the metal sulfides prior to the reaction runs ((a), (f), and (k) for MnS; (b), (g), and (l) for FeS; (c), (h), and (m) for CoS; (d), (i), and (n) for NiS; (e), (j), and (o) for CuS). Parentheses in (f)–(o) denote hexagonal crystal planes indigenous to the metal sulfides. Diffractions of the metal sulfides in (f)–(o) were in accordance to those of their XRD patterns simulated (JCPDF No. of 03-065-3413 for MnS; 01-076-0962 for FeS; 03-065-8977 for CoS; 03-065-3419 for NiS; 01-079-2321 for CuS).

3. Results and discussion

3.1. Properties of catalysts

Metal sulfide catalysts were prepared via hydrothermal or solvothermal synthesis, whose specifics were described in Methods. Bulk structural trait of the catalysts was analyzed via X-ray diffraction (XRD) experiments. As shown in Fig. 2(k)–(o), their XRD patterns revealed typical hexagonal diffractions and were in good agreement with those simulated. Polycrystalline feature of the catalysts demonstrated above was also consistent to their surfaces. This was corroborated by selected area electron diffraction (SAED) patterns of the catalysts, where their surfaces exhibited dots assigned to their intrinsic hexagonal facets (Fig. 2(f)–(j)). Indeed, their surfaces comprised of multiple facets distinguishable one another, resulting partially from different atom connectivities indigenous to the metal sulfides or different synthetic conditions (Fig. 1(b)). These catalysts, however, were anticipated to reduce any potential geometrical effect on their catalytic H_2O_2 cleavage consequences because of their identical hexagonal crystal system.

Morphological character of the catalysts was also analyzed using high-resolution transmission electron microscopy (HRTEM) images, in which the catalysts were mainly composed of 2–10 μm-sized aggregates with lattice fringes, while showing no discernable morphological shape (Fig. 2(a)–(e)). In addition, N_2 physisorption experiments of the catalysts gave clue that these mostly provided little porosities, as supported by Brunauer-Emmett-Teller surface areas (S_{BET}) of $\leq 10\, m^2\, g_{CAT}^{-1}$ and Barrett–Joyner–Halenda pore volumes (V_{BJH}) of $\leq 0.03\, cm^3\, g_{CAT}^{-1}$ except for CoS. CoS provided S_{BET} of $25\, m^2\, g_{CAT}^{-1}$ and V_{BJH} of $0.13\, cm^3\, g_{CAT}^{-1}$. Therefore, CoS could potentially show the greatest H_2O_2 scission performance among all metal sulfides only if CoS dispersed Lewis acidic sites, whose strength and quantity per unit surface area were comparable throughout all metal sulfides. However, in conjunction with the similarity of the morphological feature among the metal sulfides, small difference in their porosities led us to suggest that any

morphological or textural effect on H_2O_2 cleavage performance of the catalysts was likely insignificant.

X-ray photoelectron (XP) spectroscopy experiments of the metal sulfides were attempted to observe their surface phases in addition to their relative abundance (Fig. S1). Obviously, the surfaces contained S-modified metal species [26–29], as evidenced by M^{2+} (M: metal) and S^{2-} species observed in M 2p $_{3/2}$ and S 2p regimes of the XP spectra throughout all metal sulfides [26–29]. In addition, the surfaces also included metal and sulfur species with a variety of phases such as Mn^{3+}/Mn^{4+} and $S_{POLY}^{2-}/S/SO_z^{2-}$ for MnS (Z = 3 or 4) [26–29]. It should not be disregarded that the surfaces might experience partial oxidation during the catalyst syntheses and thus provided high-valent metal species (i.e., M^{3+} or M^{4+}) [25,30]. These metal species, however, might be also assigned as defective yet Lewis acidic sites to potentially catalyze H_2O_2 cleavage, as conjectured based our previous works on metal vanadate [18]. Hence, XP spectra of the catalysts seemed insufficient to conclude 'Which metal sulfide does provide a surface with Lewis acidity desired to interact with H_2O_2?'

Conversely, CO-pulsed chemisorption experiment was reported as one of powerful techniques to selectively quantify CO-accessible, Lewis acidic (or defective) sites included in the metal sulfides [6], metal vanadates [18,19,22], metal phosphides [17] and thus was also utilized in this work. Among all catalysts, MnS provided the largest amount of CO-accessible sites per gram of catalyst (N_{CO} of 0.45 ($\pm$ 0.01) μmol_{CO} g_{CAT}^{-1}). Conversely, FeS and CoS only provided N_{CO} values of 0.06 ($< \pm$ 0.01) μmol_{CO} g_{CAT}^{-1} and 0.03 ($< \pm$ 0.01) μmol_{CO} g_{CAT}^{-1}, respectively. These results were coincident with the structural analysis of the metal sulfide single crystals, as stated above. CuS, however, only provided N_{CO} of 0.13 ($\pm$ 0.01) $\mu molCO$ g_{CAT}^{-1}, even with the inclusion of $Cu^{\delta+}$ sites open to CO. In addition, although NiS only incorporates coordinatively-saturated, closed $Ni^{\delta+}$ sites in its structure, it did provide N_{CO} of 0.43 ($\pm$ 0.01) $\mu molCO$ g_{CAT}^{-1}, which was comparable to that of MnS. This could result from the defects present in NiS surface, which suggested defective sites innate to the metal sulfides were
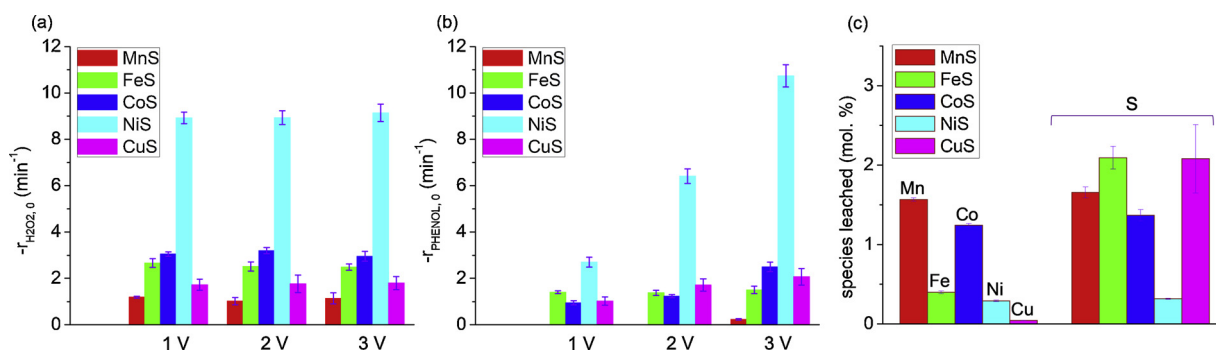
Fig. 3. (a) Background-subtracted initial H_2O_2 scission rates (-$r_{H2O2,\ 0}$) of the metal sulfides under various quantities of H_2O_2. 1.5 mmol, 2.5 mmol, or 4.0 mmol of H_2O_2 was utilized as control to simulate phenol degradation runs at 1 V, 2 V, or 3 V. (b) Background-subtracted initial phenol degradation rates (-$r_{PHENOL,\ 0}$) of the metal sulfides at various electric potentials. -$r_{PHENOL,\ 0}$ values of MnS at 1 and 2 V were omitted because these were near zero post background corrections. (c) Amounts of metal or sulfur species leached from the surfaces of the metal sulfides during phenol degradation runs at 3 V. Reaction condition of (a): 0.2 g (or 0 g) of catalyst; 0.2 mol of Na_2SO_4; 4.0 mmol (or 2.5 mmol or 1.5 mmol) of H_2O_2; 100 mL of de-ionized water; 25 °C. Reaction condition of (b) and (c): 0.2 g (or 0 g) of catalyst; 0.2 mol of Na_2SO_4; 0.1 mmol of phenol; 100 mL of de-ionized water; 25 °C; 1, 2, or 3 V.

another factor to weigh up for clarifying their H_2O_2 scission trend. Nonetheless, CO-accessible, Lewis acidic sites innate to the MS catalysts were quantified isothermally (i.e., at 40 °C). These CO-accessible sites, hence, could allow for investigating the effect of Lewis acidic strength of a specific metal site on its H_2O_2 cleavage performance via kinetic assessment, through which initial H_2O_2 scission (or initial phenol degradation) rates of the catalysts were extracted. This was because such kinetic results of the catalysts were obtained at 25 °C and were normalized with respect to their corresponding N_{CO} values for comparison.

3.2. H_2O_2 evolution

For the kinetic investigation of catalytic H_2O_2 scission, its elementary steps on (or near) the catalyst surfaces were initially established such as H_2O_2 evolution, H_2O_2 adsorption, surface reaction to form ˙OH, and ˙OH desorption. Reaction protocols and conditions were specified in Methods and figure captions, respectively. We first inspected H_2O_2 evolution because this could be catalytically driven by the surfaces and therefore might direct the resulting lumped H_2O_2 scission rates obtained via kinetic assessment. H_2O_2 evolution runs at various electric potentials (1, 2, and 3 V) were performed under the identical conditions to those used to decompose phenol except for the absence of phenol. Interestingly, H_2O_2 productivity was significantly directed by catalytic or electronic properties inherent to S-modified metal species ($M^{\delta+}$). This was demonstrated by Fig. S2(a)–(c) showing H_2O_2 concentrations increased rapidly and were dependent on the type of $M^{\delta+}$ during the initial hour of the reaction runs at 1–3 V. 2 electrons (e^-) were reported to participate in yielding H_2O_2 on (or near) the cathode via the reaction of $2H^+ + O_2 + 2e^- \rightarrow H_2O_2$ [3,6], during which $M^{\delta+}$ had a great chance to affect the electric current, which in turn might influence on e^- quantity. This could be evidenced by the electric conductivities of the reaction solutions recorded during the initial 2 h of the reaction runs at 1 V and 3 V (Fig. S2(d)–(e)). Blank runs (i.e., a reaction run in the absence of catalyst) showed smaller electric conductivities than the reaction runs in the presence of the catalysts, thereby providing lower H_2O_2 productivities at 1 V and 3 V. These were in contrast to the reaction runs with catalysts, where the metal sulfide with a higher electric conductivity of its reaction solution led to a greater H_2O_2 productivity. Interestingly, CuS yielded H_2O_2 less productively than FeS, CoS, and NiS although their electric conductivities were comparable at 3 V. This might potentially result from $Cu^{\delta+}$ sites less favorable to catalyze H_2O_2 production at 3 V. Of note, the quantities of H_2O_2 generated during the reaction runs were 5–15 times, 10–20 times, and 10–40 times the quantities of phenol used for its decomposition runs at 1 V, 2 V, and 3 V, respectively. Of additional note, H_2O_2 quantities produced during the reaction runs grew promptly and were almost saturated within an hour

of the reaction runs. This was in contrast to the quantities of phenol that were continuously reduced over 8 h of the reaction runs. These could provide evidence that H_2O_2 evolution must not be the rate-determining step in catalyzing H_2O_2 scission on the metal sulfides.

3.3. H_2O_2 scission

We then performed catalytic H_2O_2 scission runs under the identical conditions to those used to degrade phenol except for the absence of phenol and electric potential. The amounts of H_2O_2 used for these reactions were determined based on the amounts of H_2O_2 saturated during H_2O_2 evolution runs (N_{H2O2}), where 0.3–1.3 mmol of N_{H2O2} was observed at 1 V, whereas a wide spectrum of N_{H2O2} values were observed at greater electric potentials such as 0.8–2.2 mmol H_2O_2 for 2 V and 1.1–3.6 mmol H_2O_2 for 3 V. As controls, 1.5 mmol, 2.5 mmol, and 4 mmol of H_2O_2 were selected for H_2O_2 scission runs to simulate 'How many H_2O_2 species were cleaved during phenol degradation runs at 1 V, 2 V, and 3 V?' Interestingly, in spite of the absence of the catalysts, H_2O_2 was indeed active and thus could be cleaved through the oxidation of the carbon-based electrodes (i.e., graphite) or the reaction of $H_2O_2 \rightarrow \ ^˙OOH + H^+ + e^-$ on the graphite electrodes [3,6,31,32]. Such background contributions were quantified via blank runs at 1 V, 2 V, and 3 V and were used to correct H_2O_2 scission performance of the catalysts for additional rigor. H_2O_2 scission abilities of the catalysts were evaluated using their initial H_2O_2 scission rates (-$r_{H2O2,0}$), whose specification was found in Methods (Fig. S3 and Table S1). In the case of the reaction runs with 4 mmol of H_2O_2 to simulate the phenol degradation runs at 3 V, NiS revealed the greatest H_2O_2 scission performance. This was demonstrated by 3–9 folds increase in -$r_{H2O2,\ 0}$, when using $Ni^{\delta+}$ as a catalytic site (Fig. 3(a)).

In addition, MnS and CuS were validated to cleave H_2O_2 via inefficient manners and therefore exhibited the smallest -$r_{H2O2,0}$ values of ˜1 min^{-1} and ˜1.5 min^{-1}, respectively. Of substantial importance, we constructed a volcano-shaped curve of -$r_{H2O2,0}$ versus metal sulfide, in which NiS was located in the middle, whereas MnS and CuS were placed at both ends. The reaction runs with 1.5 mmol of H_2O_2 or 2.5 mmol H_2O_2 were also conducted to simulate the phenol degradation runs at 1 V or 2 V (Fig. 3(a)). Albeit the amounts of H_2O_2 were reduced from 4 mmol to 2.5 mmol or 1.5 mmol for these reactions, the resulting -$r_{H2O2,0}$ values for all catalysts were almost invariant. These reaction runs also exhibited the identical -$r_{H2O2,0}$ trend to that found in the reaction runs with 4 mmol of H_2O_2. In addition to revealing the largest H_2O_2 conversions among all catalysts throughout 8 h of the reaction runs (Fig. S3), $Ni^{\delta+}$ sites of NiS validated themselves as a promising catalytic phase for efficiently fragmenting H_2O_2. The periodic H_2O_2 scission trend derived from these experiments, however, was deemed

entangled because a primary factor to govern this trend was highly lumped. For instance, the greatest $-r_{H2O2,0}$ observed in $Ni^{\delta+}$ sites was because of 1) its adsorption energy barrier optimized to interact with H_2O_2, 2) its smallest energy barrier required to proceed catalytic $\cdot$OH production, or 3) its smallest desorption energy barrier required to release $\cdot$OH.

3.4. Phenol degradation

We then conducted phenol degradation runs at various electric potentials (i.e., 1–3 V). The purposes of these runs were 1) to better understand surface dynamics during catalytic H_2O_2 scission on $M^{\delta+}$ sites and 2) to observe their ultimate phenol degradation performance. Prior to conducting these runs, we needed to ensure that phenol decomposition was greatly directed by $\cdot$OH species, resulting from $M^{\delta+}$-mediated H_2O_2 scission. Tert-butyl alcohol (TBA) was known as a potent scavenger to terminate $\cdot$OH via the reaction of $C_4H_9OH + \cdot OH \rightarrow C_4H_9O\cdot + H_2O$ [33,34] and thus was used to verify our claim discussed above. Scavenging experiments were performed identically to phenol degradation runs at 3 V except for the addition of TBA. The amount of TBA used for these reactions was determined based on two possible reaction routes of $M^{\delta+} + H_2O_2 \rightarrow M^{(\delta+1)+} + \cdot OH + OH^-$ [1–3,6] and $M^{\delta+} + H_2O_2 \rightarrow M^{\delta+} + \cdot OH + \cdot OH$ [35]. We therefore set the amount of TBA twice the amount of H_2O_2 used during the reaction runs to simulate the phenol degradations at 3 V (i.e., 8 mmol). Phenol conversions of all catalysts were $\leq \tilde{}5\%$ up to 8 h of the reaction runs and were comparable to that of blank run, where no catalyst was used (Fig. S4). This could be an indicative that the major source to degrade phenol was $\cdot$OH species generated on $M^{\delta+}$ sites.

Of interest was that the blank run exhibited its phenol conversion (X_{PHENOL}) of $\tilde{}35\%$ after 8 h of the reaction run and reduced its X_{PEHNOL} to $\tilde{}5\%$ upon the addition of TBA scavenger. (See filled black and empty black squares in Fig. S4.) It was reported that the blank run could initially produce $\cdot$OH on the graphite anode via H_2O oxidation (* in Fig. 1(a)), yet, lost $\cdot$OH due to its chemical lability to react with the graphite [1,36]. This could result in the formation of oxygen species chemisorbed on the graphite anode (O_α) and active to oxidize phenol even in the absence of the catalyst (denoted as anodic phenol oxidation) [1,36]. Therefore, it was likely that TBA used during the blank run might quench $\cdot$OH species produced via anodic H_2O oxidation, considerably decrease the amount of O_α utilized to perform anodic phenol oxidation, thereby reducing phenol conversions in comparison with those of the blank run without TBA. Of note, the background contribution mentioned above (i.e., X_{PHENOL} of $\tilde{}35\%$ in the blank run) was considerable and therefore was eliminated to precisely evaluate catalytic consequences of $M^{\delta+}$ sites to ultimately decompose phenol. These were also evaluated using initial phenol degradation rates of $M^{\delta+}$ sites ($-r_{PHENOL,0}$), whose determination was found in Methods (Fig. S5 and Table S1). The phenol degradation runs at 3 V revealed similar periodic trend to that of catalytic H_2O_2 scission with 4 mmol of H_2O_2 (Fig. 3(b)).

Of additional interest was the phenol degradation runs at 1 V, where $-r_{PHENOL,0}$ values of all $M^{\delta+}$ sites were far smaller than those of the phenol degradation runs at 3 V, albeit showing the consistent periodic trend (Fig. 3(b)). Of importance, we conjectured that the alteration of an electric potential could greatly affect the surface energies of the catalysts immobilized on the cathode during the phenol decomposition runs at 1–3 V. This postulation was partially validated by the phenol decomposition runs at 4 V (not shown), during which quite a few of the coated catalysts were escaped from the cathode due potentially to a large electric potential. Therefore, it was highly likely that greater electric potential made the catalytic surface less amicable to adsorb H_2O_2 or more favorable to desorb $\cdot$OH during phenol degradation runs. If surface reaction to produce $\cdot$OH were the rate-determining step, $-r_{PHENOL,0}$ values of a specific catalyst should be identical even with the change in electric potentials. This was because an electric potential was presumed to primarily affect catalytic surface energy, as stated above.

Given that $-r_{PHENOL,0}$ of the catalyst was the significant function of electric potential, surface $\cdot$OH production step should not be regarded as the rate-determining step. In addition, if H_2O_2 adsorption on $M^{\delta+}$ sites were the rate-determining step, $-r_{PHENOL,\ 0}$ values of a specific catalyst should be greater at lower electric potentials. This was because lower electric potential could allow for the adsorption of greater H_2O_2 quantity on $M^{\delta+}$ site per unit time, thereby accelerating its H_2O_2 turnover cycle to form $\cdot$OH. The trend depicted above was opposite to the trend of $-r_{PHENOL,0}$ versus electric potential in Fig. 3(b). This could corroborate that H_2O_2 adsorption should not be the rate-determining step. The increase in $-r_{PHENOL,0}$ value of a specific catalyst at greater electric potential was obvious throughout all catalysts. This provided concrete evidence that greater electric potentials tended to desorb larger quantity of $\cdot$OH species from $M^{\delta+}$ site per unit time and could facilitate/direct overall phenol degradation performance.

3.5. Key factors

NiS apparently showed the best $-r_{PHENOL,0}$ values and phenol conversions among the catalysts throughout all electrical potentials (Fig. S5). One of factors to consider for sustaining electro-Fenton reaction was reported to minimize the leaching of active sites inherent to the catalytic solids [1–6]. NiS could provide the best tolerance against the leaching of its components during the reaction run. This was evidenced by the quantities of metal and sulfur (S) contents present in the reaction solutions post the reaction runs, both of which were measured via analytical techniques specified in Methods. These analyses showed that NiS leached the fewest numbers of metal (Ni) and S species among all catalysts post phenol degradation runs at 3 V (Fig. 3(c)). These experiments provided compelling evidence that NiS was superior to the others in fragmenting H_2O_2 for the ultimate decomposition of phenol.

Another factor to consider for sustaining electro-Fenton reaction was reported to proceed the reaction via heterogeneous catalysis for assuring multiple utilization of the catalytic solids [1–6]. Filtration runs were carried out to inspect whether the catalysts degraded phenol via heterogeneous catalytic H_2O_2 scission (Fig. 4) [6,25]. These control runs were performed under the identical conditions to those used for the phenol degradation at 3 V except that the catalyst-coated cathode was exchanged with the catalyst-uncoated analogue after an hour of the reaction runs (Fig. 4). If H_2O_2 cleavage occurred via heterogeneous catalysis, one should observe that phenol concentrations decomposed at 1–8 h of the reaction runs were comparable through all reaction runs including the blank run [6,25]. Obviously, all reactions exhibited similar magnitude of phenol concentrations lost during 1–8 h of the reaction runs (C^*_{PHENOL}). These experiments could substantiate the heterogeneous catalytic nature of the metal sulfides to fragment H_2O_2.

The other factor to consider for sustaining electro-Fenton reaction was reported to locate the H_2O_2 scission domain appropriate for the catalyst to balance its activity and stability. For this study, we chose NiS due to its appreciable ability as a H_2O_2 scissor, tested its capability to decompose phenol at 3 V under acidic or basic conditions by adjusting pH value of the reaction mixtures to 3 or 10. We then contrasted the resulting $-r_{PHENOL,0}$ values (activity) and the leached Ni/S quantities (stability) with those obtained at pH value of 7. $-r_{PHENOL,0}$ value at pH$\tilde{}3$ was comparable to that at pH$\tilde{}7$ (Figs. 5(b) and S6). In addition, the reaction runs at pH of 3 and 7 leached negligible amount of S species (< 0.3 mol. %, Fig. 5(a)). These results might suggest that acidic condition could favor to achieve high activity and stability for NiS when degrading phenol. The amount of Ni species leached at pH$\tilde{}3$ ($\tilde{}1.4$ mol. %), however, was far greater than that leached at pH$\tilde{}7$ ($\tilde{}0.3$ mol. %, Fig. 5(a)). This was also in close line with the XRD pattern of NiS post the reaction run at pH$\tilde{}3$, which revealed the diffractions assigned as elemental sulfur, while lacking the facets assigned as metallic Ni (Fig. S6(c)). We postulated that under acidic condition, NiS underwent its dissolution to release $Ni^{\delta+}$ and S^{2-} species, among which a few S^{2-} species might be oxidized to form elemental S species. In addition, we
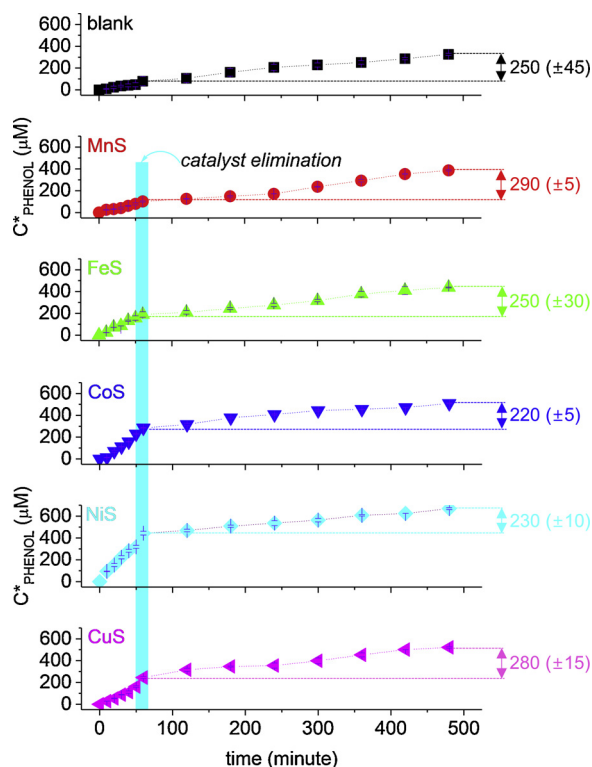
Fig. 4. Phenol degradation profiles (amount of phenol decomposed (C*PHENOL) versus time) obtained through the filtration runs without or with the use of the metal sulfides. In the blank run, the cathode uncoated with a metal sulfide catalyst served to monitor phenol degradation performance. Reaction condition: 0.2 g (or 0 g) of catalyst; 0.2 mol of Na₂SO₄; 0.1 mmol of phenol; 100 mL of de-ionized water; 25 °C; 3 V.
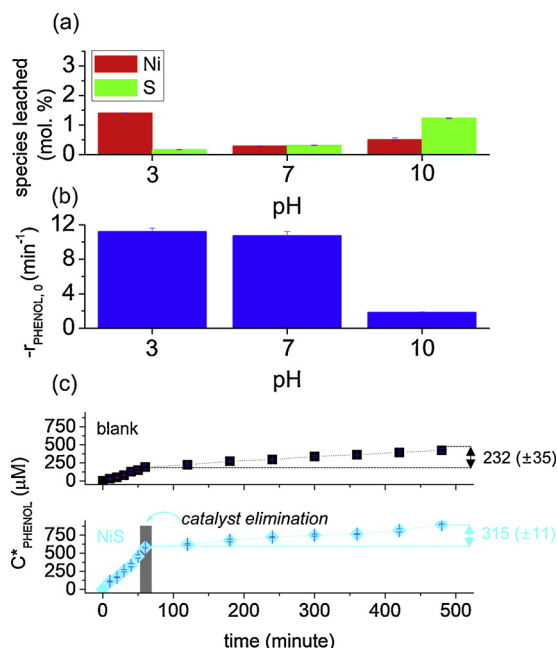

Fig. 5. (a) Amounts of Ni or S species leached from NiS surfaces during the phenol degradation runs at pH of 3, 7, and 10. (b) Background-subtracted initial phenol degradation rates (-$r_{PHENOL,0}$) obtained through the runs on NiS at pH of 3, 7, and 10. (c) Phenol degradation profiles (amount of phenol decomposed (C*PHENOL) versus time) obtained through the filtration runs without or with the use of NiS at pH of 3. In the blank run, the cathode uncoated with NiS served to monitor phenol degradation performance at pH of 3. Reaction condition: 0.2 g (or 0 g) of catalyst; pH of 3 (or 7 or 10); 0.2 mol of Na₂SO₄; 0.1 mmol of phenol; 100 mL of de-ionized water; 25 °C; 3 V.

also conjectured that such a high -$r_{PHENOL,0}$ value at pH~3 was mainly ascribed to the water-soluble, unsupported $Ni^{\delta+}$ species to catalyze H_2O_2 cleavage via homogeneous catalysis. This could be substantiated by the filtration run of NiS at pH~3, whose experimental conditions were identical to those shown in Fig. 4. Apparently, the amount of phenol consumed post the removal of NiS (i.e., 1–8 h) was ~80 μM greater than that obtained during blank run at 1–8 h (Fig. 5(c)).

In contrast to the -$r_{PHENOL,0}$ values at pH ≤ 7, -$r_{PHENOL,0}$ value at pH~10 was about one-eighth of those at pH ≤ 7 (Fig. 5(b)). In addition, NiS lost substantial quantity of S^{2-} during the reaction run at pH~10 (~1.2 mol. %), whose quantity was marginal in comparison with those lost during the reaction runs at pH of ≤ 7 (i.e., ≤ ~0.3 mol. %, Fig. 5(a)). Similar to NiS at pH of 3, NiS at pH of 10 also experienced its structural dissolution to liberate $Ni^{\delta+}$ and S^{2-} species, each of which could interact with OH- (prevalent under a basic pH) and undergo e-liberation, respectively. These species, hence, were converted into Ni(OH)₂ and elemental S species, which was evidenced by the XRD pattern of NiS post the reaction run at pH~10 (Fig. S6(c)). We presumed that such a low -$r_{PHENOL,0}$ value at pH~10 might be ascribed to Ni(OH)₂ precipitate that potentially hampered the interactions between H_2O_2 and the supported $Ni^{\delta+}$ species of NiS, thereby decelerating ˙OH production. Given all the experimental results at pH~3 and pH~10, it could be concluded that the acidic and basic conditions could expedite the structural collapse of NiS and therefore were harmful to attain moderate activity or stability for NiS in decomposing phenol. These experimental runs, however, could offer an effective reaction domain, where NiS might sustainably degrade phenol at or near pH-neutral conditions.The last factor to consider for sustaining electro-Fenton reaction was reported to secure the long-term usage of the catalytic solids [1–6]. Again, while selecting NiS because of its outstanding performance to degrade phenol, we diagnosed its catalytic recyclability at 3 V

at pH-neutral condition. The catalyst post the reaction was filtered, rinsed to remove a binder used for its immobilization on the cathode, dried, and piled up until we had a sufficient amount of catalyst for the next recycle run. NiS converted ~80% of the phenol used during the 1st run, yet, reduced its X_{PHENOL} value to ~ 65% during the 3rd run (Fig. S7(a)), throughout which NiS leached minute quantities of Ni and S species (i.e., < 0.5 mol. % in Fig. 6(a)). In the sole basis of these two analyses, NiS seemed to show moderate catalytic stability to degrade phenol at pH~7. This, however, might be contradicted by -$r_{PHENOL,0}$ values of NiS during the recycle runs, where -$r_{PHENOL,0}$ values decreased continuously from ~11 min⁻¹ to ~6 min⁻¹, as shown in Figs. 6(b) and S7(b). The amounts of CO-accessible sites (N_{CO}) of NiS post each of the recycle runs were also interesting because these N_{CO} values increased gradually up to the 3rd run (Fig. 6(c)).

This could be attributed to the reduction of NiS particulates by e⁻ during the recycle runs, some of which eventually turned into metallic Ni and elemental S. This was evidenced by the XRD pattern of NiS post the 3rd run, which showed diffractions assigned as Ni, S, or NiS (Fig. S7(c)). Metallic Ni was reported to also provide CO-accessible sites [20,21], yet, was assumed not to catalyze H_2O_2 evolution or H_2O_2 scission. This presumption was demonstrated by H_2O_2 evolution, H_2O_2 scission, and phenol degradation runs on metallic Ni, all of which exhibited similar performance to that of the corresponding blank runs (Fig. S7(d)–(f)). In addition, a series of control runs on elemental S also verified that its H_2O_2 productivity and phenol degradation performance was even lower than that of the corresponding blank runs, partially resulting from the significant electro-resistive feature of the elemental S [37,38] (Fig. S7(d)–(f)). Therefore, it was highly convincing that despite ostensibly exhibiting moderate catalytic recyclability, NiS suffered from its further reduction to form dummy Ni species accessible to CO, thereby reducing -$r_{PHENOL,0}$ values during each of the recycle runs.
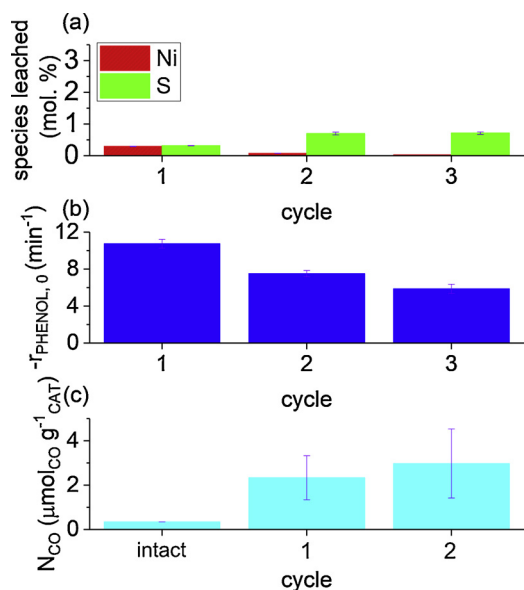
Fig. 6. (a) Amounts of Ni or S species leached from NiS surface during the recycle runs. (b) Background-subtracted initial phenol degradation rates ($-r_{PHENOL,0}$) obtained through the recycle runs on NiS. (c) Amounts of CO-accessible sites (N_{CO}) innate to NiS surfaces prior to or post the recycle runs. Reaction condition: 0.2 g (or 0 g) of catalyst; 0.2 mol of Na_2SO_4; 0.1 mmol of phenol; 100 mL of de-ionized water; 25 °C; 3 V.

4. Conclusions

In this study, we have experimentally explored the traits of ubiquitous S-modified metal species ($M^{\delta+}$, $\delta \leq 2$) in catalyzing H_2O_2 fragmentation to form powerful oxidant, ·OH. For this investigation, nearly non-porous metal sulfides with the *iso*-structural formula of MS were synthesized with the use of the metals, which were located at the identical period with the different groups in the periodic table (M = Mn, Fe, Co, Ni, or Cu). Even with the potential minimization of textural or geometrical effects on the catalytic properties, the resulting $M^{\delta+}$ species were anticipated to reveal variant, unique Lewis acidic features in terms of their accessibilities to and their binding strengths with H_2O_2 or ·OH. $M^{\delta+}$ species innate to the MS catalysts, however, could be characterized using CO as a probe molecule (CO-pulsed chemisorption), which allowed for the quantification of Lewis acidic $M^{\delta+}$ species inherent to the MS catalysts accessible to CO (N_{CO}) under the identical temperature close to 25 °C (i.e., reaction temperature).

To investigate the periodic trend and the rate-determining step of the MS catalysts whose N_{CO} values were known, these catalysts were exposed to such regulated reaction environments as to provide background-corrected kinetic dataset including initial H_2O_2 scission rates ($-r_{H2O2,0}$) and initial degradation rates of a model compound, phenol ($-r_{PHENOL,0}$). The periodic trend could be found in the MS catalysts, among which NiS showed the greatest values of $-r_{H2O2,0}$ and $-r_{PHENOL,0}$, potentially resulting from its Lewis acidic nature proper to readily desorb ·OH species. NiS ($Ni^{\delta+}$), hence, was positioned in the middle of the volcano-shape curves of $-r_{H2O2,0}$ (or $-r_{PHENOL,0}$) versus $M^{\delta+}$. In addition, a series of phenol degradation runs on the MS catalysts showed promoted $-r_{PHENOL,0}$ values at greater electric potentials, which corroborated that ·OH liberation from $M^{\delta+}$ species could be the rate-determining step for catalytic H_2O_2 fragmentation.

Along with the investigation of the fundamental aspects of the MS catalysts in accelerating H_2O_2 scission, we also diagnosed their applied aspects to sustain the degradation of the recalcitrant pollutants. NiS was demonstrated to significantly suppress the leaching of Ni and S species during the phenol degradation, while fragmenting H_2O_2 via heterogeneous catalysis at pH-neutral condition, as verified by the filtration

study. Nonetheless, NiS showed its structural dissociation to form Ni and S and therefore continuously reduced its $-r_{PHENOL,0}$ values throughout the recycle runs. As of now, we conjecture that the chemical susceptibility of NiS during H_2O_2 scission can be complemented by its fusion with chemically-robust, secondary transition metals to generate bimetallic sulfides (e.g., W and Mo). In addition, although providing compelling evidence to support ·OH desorption from $M^{\delta+}$ species was the rate-determining step, we are lacking the accurate information associated with Lewis acidities of $M^{\delta+}$ species and their reaction coordinates to detail energy barrier on each elementary step. These will be elaborated via computation to systematically simulate surface H_2O_2 scission dynamics on well-defined MS facets.

Author contributions

Dr. J. Kim established the motivation and hypotheses for this work, designed the experiments, refined/interpreted the data, and drafted/revised the manuscript. Y. J. Choe performed the experiments. Dr. S.H. Kim, Dr. S.-C. Lee, and Dr. S. Bhattacharjee interpreted the data and commented on the manuscript.

Appendix A. Supplementary data

Supplementary material related to this article can be found, in the online version, at doi:https://doi.org/10.1016/j.apcatb.2019.04.016.

References

[1] E. Brillas, I. Sirés, M.A. Oturan, Electro-fenton process and related electrochemical technologies based on Fenton's reaction chemistry, Chem. Rev. 109 (2009) 6570–6631.

[2] J. Kim, Y.J. Choe, S.H. Kim, K. Jeong, Enhancing the decomposition of refractory contaminants on SO_4^{2-}–functionalized iron oxide to accommodate surface $SO_4^{·-}$ generated via radical transfer from ·OH, Appl. Catal. B 252 (2019) 62–76.

[3] F.C. Moreira, R.A.R. Boaventura, E. Brillas, V.J.P. Vilar, Electrochemical advanced oxidation processes: a review on their application to synthetic and real wastewaters, Appl. Catal. B 202 (2017) 217–261.

[4] L. Zhao, Y. Chen, Y. Liu, C. Luo, D. Wu, Enhanced degradation of chloramphenicol at alkaline conditions by S(-II) assisted heterogeneous Fenton-like reactions using pyrite, Chemosphere 188 (2017) 557–566.

[5] W. Liu, Y. Wang, Z. Ai, L. Zhang, Hydrothermal Synthesis of FeS_2 as a High-Efficiency Fenton Reagent to Degrade Alachlor via Superoxide-Mediated Fe(II)/Fe (III) Cycle, ACS Appl. Mater. Interfaces 7 (2015) 28534–28544.

[6] Y.J. Choe, J.Y. Byun, S.H. Kim, J. Kim, Fe_3S_4/Fe_7S_8-promoted degradation of phenol via heterogeneous, catalytic H_2O_2 scission mediated by S-modified surface Fe^{2+} species, Appl. Catal. B 233 (2018) 272–280.

[7] L. Guo, F. Chen, X. Fan, W. Cai, J. Zhang, S-doped α-Fe_2O_3 as a highly active heterogeneous Fenton-like catalyst towards the degradation of acid orange 7 and phenol, Appl. Catal. B 96 (2010) 162–168.

[8] J. Du, J. Bao, X. Fu, C. Lu, S.H. Kim, Mesoporous sulfur-modified iron oxide as an effective Fenton-like catalyst for degradation of bisphenol A, Appl. Catal. B 184 (2016) 132–141.

[9] A. Arunchander, S.G. Peera, A.K. Sahu, Self-assembled manganese sulfide nanostructures on graphene as an oxygen reduction catalyst for anion exchange membrane fuel cells, ChemElectroChem 4 (2017) 1544–1553.

[10] X. Wang, Q. Xiang, B. Liu, L. Wang, T. Luo, D. Chen, G. Shen, TiO_2modified FeS nanostructures with enhanced electrochemical performance for lithium-ion batteries, Sci. Rep. 3 (2013) 2007.

[11] M. Lei, X.L. Fu, Y.B. Zhang, H.J. Yang, Y.T. Huang, L. Zhang, Y.G. Wang, Synthesis of CoS nanoplates and their ferromagnetic properties, Mater. Lett. 71 (2012) 11–14.

[12] S. Liu, Q. Shi, J. Tong, S. Li, M. Li, Controlled synthesis of spherical α-NiS and urchin-like β-NiS microstructures, J. Exp. Nanosci. 9 (2014) 475–481.

[13] M. Saranya, C. Santhosh, R. Ramachandran, P. Kollu, P. Saravanan, M. Vinoba, S.K. Jeong, A.N. Grace, Hydrothermal growth of CuS nanostructures and its photocatalytic properties, Powder Technol. 252 (2014) 25–32.

[14] E. Capetti, A.M. Ferretti, V. Dal Santo, A. Ponti, Surfactant-controlled composition and crystal structure of manganese(II) sulfide nanocrystals prepared by

solvothermal synthesis, Beilstein J. Nanotechnol. 6 (2015) 2319–2329.

[15] M. Ohmasa, M. Suzuki, Tak, Y. Eacute, Uchi, A refinement of the crystal structure of covellite, CuS, Miner. J. 8 (1977) 311–319.

[16] S.J.K. Kuhn, M.K. Parker, D.S. dela Cruz, C. McGuire, M.A. Chance, W.M. Li, Li Debeer-Schmitt, L. Ermentrout, J. Littrell, K.C. Eskildsen, M.R. Sefat, A. S, Structure and property correlations in FeS, Phys. C 534 (2017) 29–36.

[17] D.J. Rensel, J. Kim, V. Jain, Y. Bonita, N. Rai, J.C. Hicks, Composition-directed $Fe_xMo_{2-x}P$ bimetallic catalysts for hydrodeoxygenation reactions, Catal. Sci. Technol. 7 (2017) 1857–1867.

[18] J. Kim, D.H. Kim, D.W. Kwon, H.P. Ha, Rational selection of $Fe_2V_4O_{13}$ over $FeVO_4$ as a preferred active site on Sb-promoted TiO_2 for catalytic NO_x reduction with NH_3, Catal. Sci. Technol. 8 (2018) 4774–4787.

[19] J. Kim, D.W. Kwon, S. Lee, H.P. Ha, Exploration of surface properties of Sb-promoted copper vanadate catalysts for selective catalytic reduction of NO_x by NH_3, Appl. Catal. B 236 (2018) 314–325.

[20] J. Kim, M.S. Abbott, D.B. Go, J.C. Hicks, Enhancing C–H bond activation of methane via temperature-controlled, catalyst–plasma interactions, ACS Energy Lett. 1 (2016) 94–99.

[21] J. Kim, D.B. Go, J.C. Hicks, Synergistic effects of plasma–catalyst interactions for CH_4 activation, Phys. Chem. Chem. Phys. 19 (2017) 13010–13021.

[22] J. Kim, S. Lee, D.W. Kwon, K.-Y. Lee, H.P. Ha, SO_3^{2-}/SO_4^{2-} functionalization-tailorable catalytic surface features of Sb-promoted $Cu_3V_2O_8$ on TiO_2 for selective catalytic reduction of NO_x with NH_3, Appl. Catal. A Gen. 570 (2019) 355–366.

[23] K. Kosaka, H. Yamada, S. Matsui, S. Echigo, K. Shishida, Comparison among the methods for hydrogen peroxide measurements to evaluate advanced oxidation processes: application of a spectrophotometric method using copper(II) ion and 2,9-Dimethyl-1,10-phenanthroline, Environ. Sci. Technol. 32 (1998) 3821–3824.

[24] T.M. Do, J.Y. Byun, S.H. Kim, An electro-Fenton system using magnetite coated metallic foams as cathode for dye degradation, Catal. Today 295 (2017) 48–55.

[25] J. Kim, N.D. McNamara, J.C. Hicks, Catalytic activity and stability of carbon supported V oxides and carbides synthesized via pyrolysis of MIL-47 (V), Appl. Catal. A Gen. 517 (2016) 141–150.

[26] M. Huang, A. Xu, H. Duan, S. Wu, Enhanced pseudocapacitance contribution to outstanding Li-storage performance for a reduced graphene oxide-wrapped FeS composite anode, J. Mater. Chem. A 6 (2018) 7155–7161.

[27] H. Chen, M.Q. Wang, Y. Yu, H. Liu, S.-Y. Lu, S.-J. Bao, M. Xu, Assembling Hollow Cobalt Sulfide Nanocages Array on Graphene-like Manganese Dioxide Nanosheets for Superior Electrochemical Capacitors, ACS Appl. Mater. Interfaces 9 (2017) 35040–35047.

[28] W. Zhu, X. Yue, W. Zhang, S. Yu, Y. Zhang, J. Wang, J. Wang, Nickel sulfide microsphere film on Ni foam as an efficient bifunctional electrocatalyst for overall water splitting, Chem. Commun. 52 (2016) 1486–1489.

[29] S. Li, Z.-H. Ge, B.-P. Zhang, Y. Yao, H.-C. Wang, J. Yang, Y. Li, C. Gao, Y.-H. Lin, Mechanochemically synthesized sub-5nm sized CuS quantum dots with high visible-light-driven photocatalytic activity, Appl. Surf. Sci. 384 (2016) 272–278.

[30] J. Kim, G.T. Neumann, N.D. McNamara, J.C. Hicks, Exceptional control of carbon-supported transition metal nanoparticles using metal-organic frameworks, J. Mater. Chem. A 2 (2014) 14014–14027.

[31] W. Xing, G. Lalwani, I. Rusakova, B. Sitharaman, Degradation of graphene by hydrogen peroxide, Part. Part. Syst. Charact. 31 (2014) 745–750.

[32] Y. Peng, H. Liu, Effects of oxidation by hydrogen peroxide on the structures of multiwalled carbon nanotubes, Ind. Eng. Chem. Res. 45 (2006) 6483–6488.

[33] P. Liu, C. Li, Z. Zhao, G. Lu, H. Cui, W. Zhang, Induced effects of advanced oxidation processes, Sci. Rep. 4 (2014) 4018.

[34] X.-R. Xu, Z.-Y. Zhao, X.-Y. Li, J.-D. Gu, Chemical oxidative degradation of methyl tert-butyl ether in aqueous solution by Fenton's reagent, Chemosphere 55 (2004) 73–79.

[35] A. Plauck, E.E. Stangland, J.A. Dumesic, M. Mavrikakis, Active sites and mechanisms for H_2O_2 decomposition over Pd catalysts, PNAS 113 (2016) E1973–E1982.

[36] M. Panizza, G. Cerisola, Direct and mediated anodic oxidation of organic pollutants, Chem. Rev. 109 (2009) 6541–6569.

[37] Y.-X. Wang, L. Huang, L.-C. Sun, S.-Y. Xie, G.-L. Xu, S.-R. Chen, Y.-F. Xu, J.-T. Li, S.-L. Chou, S.-X. Dou, S.-G. Sun, Facile synthesis of a interleaved expanded graphite-embedded sulphur nanocomposite as cathode of Li–S batteries with excellent lithium storage performance, J. Mater. Chem. 22 (2012) 4744–4750.

[38] D. Bresser, S. Passerini, B. Scrosati, Recent progress and remaining challenges in sulfur-based lithium secondary batteries – a review, Chem. Commun. 49 (2013) 10545–10562.